

# Quantum simulations of localization effects with dipolar interactions

Gonzalo A. Álvarez,<sup>1,2,\*</sup> Robin Kaiser,<sup>3,†</sup> and Dieter Suter<sup>2,‡</sup>

<sup>1</sup>*Department of Chemical Physics, Weizmann Institute of Science, Rehovot, 76100, Israel*

<sup>2</sup>*Fakultät Physik, Technische Universität Dortmund, D-44221, Dortmund, Germany*

<sup>3</sup>*Université de Nice Sophia Antipolis, CNRS, Institut Non-Linéaire de Nice, France*

(Dated: November 2, 2018)

Quantum information processing often uses systems with dipolar interactions. We use a nuclear spin-based quantum simulator, to study the spreading of information in such a dipolar-coupled system and how perturbations to the dipolar couplings limit the spreading, leading to localization. In [Phys. Rev. Lett. **104**, 230403 (2010)], we found that the system reaches a dynamic equilibrium size, which decreases with the square of the perturbation strength. Here, we study the impact of a disordered Hamiltonian with dipolar  $1/r^3$  interactions. We show that the expansion of the coherence length of the cluster size of the spins becomes frozen in the presence of large disorder, reminiscent of Anderson localization of non-interacting waves in a disordered potential.

## I. INTRODUCTION

The control of quantum mechanical systems is continuously gaining interest in recent years [1–8], mainly triggered by the pursuit of quantum information processing and quantum simulations, which both have the potential of solving computational problems more efficiently than classical computers [9–11]. The realization of this potential requires precise control of large quantum systems [12]. Controlling small quantum systems has been explored extensively over the last years [1–8, 13], but control of large quantum systems is still very challenging. The simulation of large quantum systems on classical computers is limited to about 20 qubits if only pure states are considered [14, 15]. The typical classical algorithms can be also extended to calculate the dynamics of mixed states if the initial state or the observables are localized in a region smaller than the complete system. This approach uses quantum parallelism of a single pure state evolution [16, 17]. Present quantum technologies do not allow complete control of large quantum states. So far large quantum systems were only addressed by using ensemble quantum simulations with nuclear magnetic resonance (NMR) experiments on solid state systems [18–20].

The main difficulties for controlling large quantum systems are the lack of individual addressing of qubits, with important efforts in progress with samples of ultracold atoms [21, 22]. For large systems decoherence is known to degrade the information contained in the quantum state [23]. Its rate increases with the size of the quantum system, making the largest systems the most susceptible to perturbations [13, 18–20, 24–28]. While these effects are known to affect the survival time of quantum information, they also affect the distance over which quantum states can be transmitted [28–38]. Imperfections or disorder

of the spin-spin couplings that drive the state transfer can induce localization of the quantum information [29, 31, 32, 34] in a process related to Anderson localization [39, 40]. Whereas disorder induced inhibition of transport of non interacting waves has been studied in various physical systems [41–45], the role of dipolar interactions is under theoretical investigation [46]. Here we study a 3D spin-network and demonstrated experimentally a similar behavior by studying the localization effects induced by the finite precision of quantum gate operations used for transferring quantum states [35, 36].

Reducing decoherence is a main step towards implementing large scale quantum computers. Several techniques have been proposed for this purpose, including dynamical decoupling [47], decoherence-free subspaces [48], and quantum error correction [49, 50]. These methods perform very well for small quantum systems [51–57], but they can be very challenging to implement in large quantum systems. However, based only on global manipulations of spins, some of these methods were successfully implemented in large quantum systems with thousands of qubits [19, 20, 27]. The decoherence times were extended by almost two orders of magnitude. Therefore, understanding the decoherence effects and their sources on large quantum systems would help to optimize the control techniques for fighting decoherence.

In this paper, we focus on understanding the impact of perturbations with dipolar disorder on large quantum systems by quantum simulations with solid state nuclear spin systems. These interactions depend on the distance  $r$  between the spins as  $1/r^3$ . In particular we study the length scale of localization induced by perturbing the Hamiltonian that drives the spreading of the information. Based on our previous results and methods developed in Refs. [35, 36], we prepared a system of nuclear spins  $1/2$ . Starting with uncorrelated spins we let them evolve into clusters of correlated spins with increasing size. By introducing a controlled perturbation to the Hamiltonian that generates these clusters, we find that the size of the system tends towards a limiting value determined by a dynamic equilibrium [35, 36]: if the cluster size is initially larger than this equilibrium value, it decreases

\* gonzalo.a.alvarez@weizmann.ac.il

† robin.kaiser@inln.cnrs.fr

‡ dieter.suter@tu-dortmund.de

under the effect of the perturbed Hamiltonian, and it increases while its size is below the stationary value. The equilibrium size decreases with increasing strength of the perturbation.

The paper is organized as follows. Section II describes the quantum simulator, the system and the initial state preparation. Section III shows the quantum simulations. It is divided in two parts: III.A. contains the unperturbed evolutions that drives the growth of the clusters, and it describes the technique for measuring the size of the clusters. In section III.B., we discuss the perturbed evolutions, we describe the perturbations and how we create them. In section IV, we discuss the dynamical equilibrium with stationary cluster-size, which is independent of the initial states with different cluster-sizes. Lastly, section V gives the conclusions.

## II. THE QUANTUM SIMULATOR

### A. System

We consider a system of equivalent spins  $I = 1/2$  in the presence of a strong magnetic field and subject to mutual dipole-dipole interaction. The Hamiltonian of the system is

$$\hat{\mathcal{H}} = \hat{\mathcal{H}}_z + \hat{\mathcal{H}}_{dip}, \quad (1)$$

where  $\hat{\mathcal{H}}_z = \omega_z \sum_i \hat{I}_z^i$  represents the Zeeman interaction with  $\omega_z = \hbar\gamma B_0$  as the Larmor frequency, and

$$\hat{\mathcal{H}}_{dip} = \frac{1}{2} \sum_{i < j} \frac{\vec{\mu}_i \cdot \vec{\mu}_j}{r_{ij}^3} - \frac{3(\vec{\mu}_i \cdot \vec{r}_{ij})(\vec{\mu}_j \cdot \vec{r}_{ij})}{r_{ij}^5} \quad (2)$$

is the dipolar interaction [58], typically found also in dipolar quantum gases [59] and Rydberg atoms [60] of growing interest in the context of quantum information science. The dipoles are  $\vec{\mu}_i = \hbar\gamma(\hat{I}_x^i, \hat{I}_y^i, \hat{I}_z^i)$  with  $\hat{I}_x^i, \hat{I}_y^i$  and  $\hat{I}_z^i$  the spin operators and  $\vec{r}_{ij}$  is the distance vector between  $\vec{\mu}_i$  and  $\vec{\mu}_j$ . In the presence of a strong magnetic field, ( $\omega_z \gg d_{ij}$ ), it is possible to truncate  $\hat{\mathcal{H}}_{dip}$  with respect to  $\hat{\mathcal{H}}_z$ . The part that does not commute has negligible effect on the evolution of the system [58], while the secular part can be written as

$$\hat{\mathcal{H}}_{dd} = \sum_{i < j} d_{ij} \left[ 2\hat{I}_z^i \hat{I}_z^j - (\hat{I}_x^i \hat{I}_x^j + \hat{I}_y^i \hat{I}_y^j) \right]. \quad (3)$$

The coupling constants are

$$d_{ij} = \frac{1}{2} \frac{\gamma^2 \hbar^2}{r_{ij}^3} (1 - 3 \cos^2 \theta_{ij}), \quad (4)$$

with  $\theta_{ij}$  the angle between the vector  $\vec{r}_{ij}$  and the magnetic field direction [58]. In a frame of reference rotating at the Larmor frequency  $\omega_z$  [58], the Hamiltonian of the

spin system reduces to  $\hat{\mathcal{H}}_{dd}$ . This kind of Hamiltonians can be also simulated with quantum gases [59].

In our system, the spins are the protons of polycrystalline adamantane and we performed all experiments on a home-built solid state NMR spectrometer with a  $^1\text{H}$  resonance frequency of  $\omega_z = 300$  MHz in Dortmund. As shown in Fig. 1, the adamantane molecule is nearly spherical and contains 16 protons. The molecules tumble rapidly and isotropically in the solid phase. This fast tumbling averages the intramolecular couplings to zero, but the interaction between the molecules remains. However, the couplings between molecules are averaged to a nonzero value that depends only on the relative position of the molecules to which the spins belong. They are not isotropic, and they have the normal orientation dependence of dipolar couplings of Eq. (4), but the distance is between the positions of the molecules, not of the nuclei. ‘‘Position’’ would in fact not be the center of mass of the molecules, but an effective position that is the result of the averaging process. Figure 1b shows a scheme of the interaction between two molecules, where the spins do not interact with spins within the molecules but they interact with all spins of the neighbor molecules. All coupling strength are averaged to the same value. However, in Fig. 1c, the coupling strength between molecules depends of their separation, as shown by arrows with different color tones, and on their the polar angle  $\theta_{ij}$  with respect to the magnetic field. The randomness of the dispersion of the distance vector  $\vec{r}$  between molecules will be the source of disorder on  $d_{ij}$ . The molecules are in a face-centered-cubic lattice, where each adamantane molecule has 12 first neighbor interactions with a distance of 6.6Å, then 6 second neighbors with a distance of 9.34Å, then 16 at a distance of 11.4Å and etc. The resonance width of the NMR resonance line, is 7.9 kHz.

### B. Initial state preparation

We perform quantum simulations starting from the high-temperature thermal equilibrium [58]. Using the notation  $\hat{I}_z = \sum_i \hat{I}_z^i$ , we can write the thermal equilibrium state as

$$\rho_0 = \exp \left\{ -\frac{\hbar\omega_z}{k_B T} \hat{I}_z \right\} / \text{Tr} \left\{ \exp \left\{ -\frac{\hbar\omega_z}{k_B T} \hat{I}_z \right\} \right\} \quad (5)$$

$$\approx \left( \hat{1} + \frac{\hbar\omega_z}{k_B T} \hat{I}_z \right) / \text{Tr} \{ \hat{1} \}. \quad (6)$$

It is convenient to exclude the unity operator  $\hat{1}$  since it does not evolve in time and does not contribute to the observable signal. The resulting state is  $\hat{\rho}_0 \propto \hat{I}_z$ . In this state, the spins are uncorrelated and the density operator commutes with the Hamiltonian  $\hat{\mathcal{H}}_{dd}$ . In order to prepare a different initial state, we wait a time longer that  $T_1$  to reinitialize the system state to  $\rho_0$ .

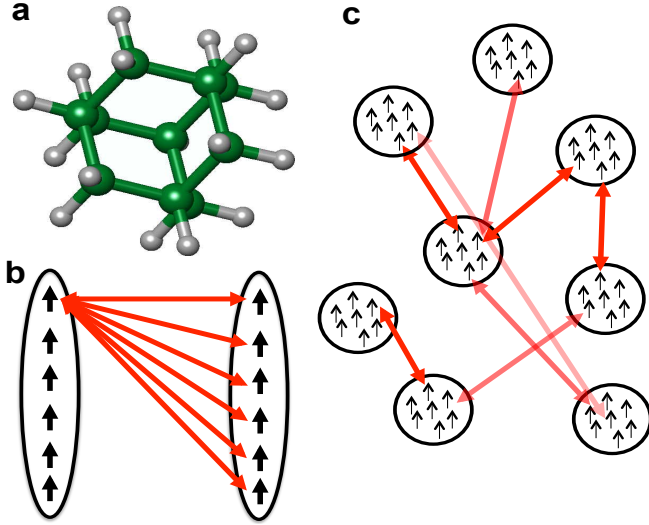


Figure 1. (Color online) Spin system. (a) Adamantane molecule with 16 protons (small gray spheres). The big green spheres are mostly  $^{12}\text{C}$  and  $^{13}\text{C}$  in natural abundance (1.1%). (b) The intramolecular interactions are averaged to zero due to very fast molecular tumbling, but the intermolecular interactions average to a non-zero value that depends of the distance between the molecules. The spins interact with spins of the other molecule with the same averaged coupling strength, as shown with arrows. (c) Schematic representation of the interactions between the molecules. The color tones of the arrows represent the variation of the coupling strength with the intermolecular distance, which varies as  $1/r_{ij}^3$ .

### III. QUANTUM SIMULATIONS

#### A. Unperturbed evolution

##### 1. Generating clusters

The initial state  $\rho_0$  of the uncorrelated spins commutes with  $\hat{\mathcal{H}}_{dd}$ . Therefore, to generate spin clusters we use an NMR method developed by Pines and coworkers [61, 62]. It is based on generating an average Hamiltonian  $\hat{\mathcal{H}}_0$  that does not commute with the thermal equilibrium state

$$\hat{\mathcal{H}}_0 = -\sum_{i<j} d_{ij} [\hat{I}_x^i \hat{I}_x^j - \hat{I}_y^i \hat{I}_y^j]. \quad (7)$$

$$= -\frac{1}{4} \sum_{i<j} d_{ij} [\hat{I}_+^i \hat{I}_+^j - \hat{I}_-^i \hat{I}_-^j]. \quad (8)$$

This Hamiltonian drives an evolution that converts the thermal initial state into clusters of correlated spins whose density operator contains terms of the form  $\hat{I}_u^i \dots \hat{I}_v^j \hat{I}_w^k$  ( $u, v, w = x, y, z$ ), where the indexes  $i, j, k$  identify the spins involved in the given cluster. The cluster-size  $K$  corresponds to the number of terms in this product, which is equal to the number of spins. The cluster size is related to the volume occupied by those spins. Ex-

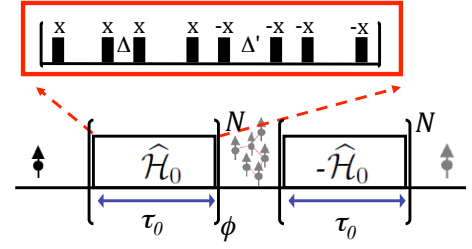


Figure 2. (Color online) Pulse sequence for the quantum simulations. (a) The effective Hamiltonian  $\hat{\mathcal{H}}_0$  is generated by the periodic sequence of  $\pi/2$  pulses. The upper part of the figure shows the basic cycle, where  $\Delta' = 2\Delta + \tau_p$ ,  $\Delta = 2\mu\text{s}$  and  $\tau_p = 2.8\mu\text{s}$  is the  $\pi/2$  pulse duration [62]. The cycle time is then  $\tau_0 = 57.6\mu\text{s}$ .

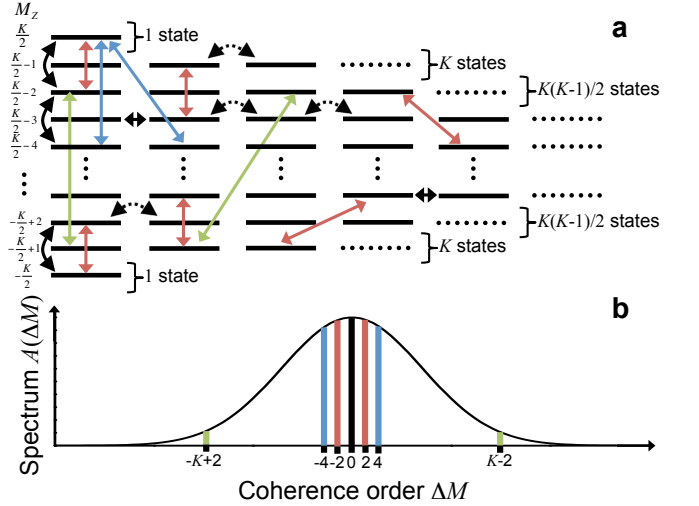


Figure 3. (Color online) Energy level scheme for a cluster of  $K$  spins. (a) The different rows correspond to Zeeman states  $|\alpha_1, \alpha_2, \dots, \alpha_K\rangle$  ( $\alpha_i = \uparrow, \downarrow$ ) with different energy determined by the quantum number  $M_z$ . The degeneracy of the levels in a row is given on the rhs of each row. The solid curved arrows show those transitions induced by the Hamiltonian  $\mathcal{H}_0$  that do not conserve  $M_z$ . The dotted curved arrows show the effect of the  $M_z$ -conserving dipolar Hamiltonian  $\mathcal{H}_{dd}$ . The straight colored arrows show the possible coherences generated by  $\mathcal{H}_0$ . (b) The number of coherences of a cluster of size  $K$  are plotted as a function of  $\Delta M$ . The colored bars give those numbers and their color code corresponds to that of panel (a).

perimentally, the Hamiltonian  $\hat{\mathcal{H}}_0$  is generated with the pulse sequence [61, 62] shown in the upper part of Fig. 2.

In the usual computational or Zeeman basis  $|\alpha_1, \alpha_2, \dots, \alpha_K\rangle$  ( $\alpha_i = \uparrow, \downarrow$ ) for a system of  $K$  spins, we write the states as  $|M_z, n_M\rangle$  where  $M_z$  is the total magnetic quantum number, *i.e.*,  $\hat{I}_z |M_z, n_M\rangle = M_z |M_z, n_M\rangle$ , and  $n_M$  distinguishes different states with the same  $M_z$ . Figure 3a shows a summary of these states, whose degeneracy is  $\max\{n_M\} = K! / [(K/2 - M_z)! (K/2 + M_z)!]$ .

The Hamiltonian  $\hat{\mathcal{H}}_0$  flips simultaneously two spins, which are separated in space and have the same orienta-

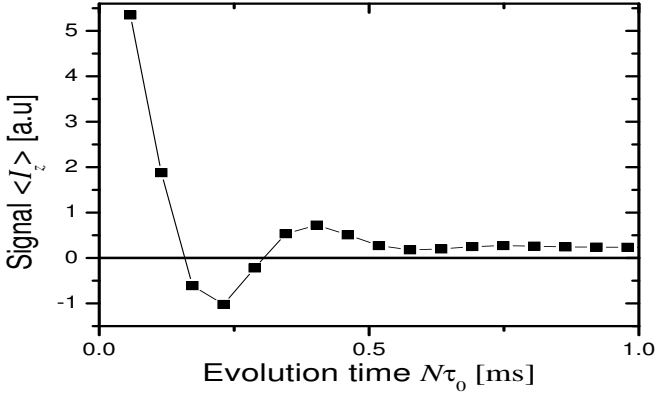


Figure 4. Time evolution driven by  $\mathcal{H}_0$  of the total magnetization  $\langle I_z(t) \rangle$  of the system as a function of time. The black squares are the unperturbed evolution, while the remaining symbols are perturbed evolutions according to the legend.

tion. Accordingly, the  $z$ -component of the magnetization  $M_z$  changes by  $\Delta M_z = \pm 2$ . This is shown with a curved solid arrow in Fig. 3a. At the same time, the number  $K$  of correlated spins changes by  $\Delta K = \pm 1$ . Therefore, starting from the thermal equilibrium state, the evolution generates a density operator where only elements  $\rho_{ij}$  with  $\Delta M = M_z(i) - M_z(j) = 2n$ ,  $n = 0, 1, 2, \dots$  are populated. Such elements  $\rho_{ij}$  are called  $\Delta M$  quantum coherences and they are represented by colored straight arrows in Fig. 3a. The different colors represent different multiple-quantum coherence (MQC) orders  $\Delta M$ . Off-diagonal elements of the density matrix with  $\Delta M = 0$  represent zero-quantum coherences and diagonal elements correspond to populations. Then, a MQC spectrum  $A(\Delta M)$  can be described by the number of coherences of the density matrix for a given  $\Delta M$ . A typical MQC spectrum is shown in Fig. 3b. The initial state  $\rho_0$  is diagonal and then  $A(\Delta M) \neq 0$  only for  $\Delta M = 0$ . However, as time evolves, different spins interact with each other and other coherence orders are excited. Then  $A(\Delta M)$  starts to spread as a manifestation of the increasing cluster-size. If we measure the evolution of the operator  $I_z$  as a function of time,  $\langle I_z(t) \rangle = \text{Tr} \{ I_z \rho(t) \}$ , its expectation value decays as a consequence of the excitation of the coherences of the density matrix that do not contribute to the observable  $\langle I_z(t) \rangle$ . The black squares in Fig. 4 show the evolution of  $\langle I_z(t) \rangle$  driven by the Hamiltonian  $\hat{\mathcal{H}}_0$ . We can see a fast decay on a time scale of  $\approx 100 \mu\text{s}$ , which is followed by a quantum beat at about  $400 \mu\text{s}$ . Then the signal saturates.

## 2. Measuring cluster sizes

To determine the average number of correlated spins in the generated clusters, we use the NMR technique developed by Baum *et al.* [62]. In a system of  $K$  spins, the number of transitions with a given  $\Delta M$  follows a binomial distribution

$$n(\Delta M, K) = \frac{(2K)!}{(K + \Delta M)! (K - \Delta M)!}. \quad (9)$$

For  $K \gg 1$ , the binomial distribution can be approximated with a Gaussian

$$n(\Delta M, K) \propto \exp\left(-\frac{\Delta M^2}{K}\right), \quad (10)$$

whose half width at  $e^{-1}$  is  $\sigma = \sqrt{K}$ . Thus, the width of the MQC spectrum reflects the cluster-size. We can determine the effective size of the spin clusters in a given state by measuring the distribution of the coherence order  $\Delta M$ . They can be distinguished experimentally by rotating the system around the  $z$ -axis: a rotation  $\hat{\phi}_z = e^{-i\phi \hat{I}_z}$  by  $\phi$  changes the density operator to

$$\hat{\rho}(\phi) = \hat{\phi}_z \hat{\rho} \hat{\phi}_z^\dagger = \sum_{\Delta M} \hat{\rho}_{\Delta M} e^{i\Delta M \phi}, \quad (11)$$

where  $\hat{\rho}_{\Delta M}$  contains all the elements of the density operator involving coherences of order  $\Delta M$ .

By following the sequence of Fig. 2, the system evolution is first described by an evolution period of duration  $N\tau_0$  under the Hamiltonian  $(\hat{\mathcal{H}}_0)_\phi = \hat{\phi}_z \hat{\mathcal{H}}_0 \hat{\phi}_z^\dagger$ , *i.e.*,

$$\begin{aligned} \hat{\rho}_0 \xrightarrow{(\hat{\mathcal{H}}_0)_\phi, N\tau_0} \hat{\rho}_\phi(N\tau_0) &= \hat{\phi}_z \hat{\rho}(N\tau_0) \hat{\phi}_z^\dagger \\ &= \hat{\phi}_z e^{-i\hat{\mathcal{H}}_0 N\tau_0} \hat{\rho}_0 e^{i\hat{\mathcal{H}}_0 N\tau_0} \hat{\phi}_z^\dagger \\ &= \sum_{\Delta M} \hat{\phi}_z \hat{\rho}_{\Delta M}(N\tau_0) \hat{\phi}_z^\dagger \\ &= \sum_{\Delta M} \hat{\rho}_{\Delta M}(N\tau_0) e^{i\Delta M \phi}. \end{aligned} \quad (12)$$

The next part of the sequence of Fig. 2 is an evolution of the same duration  $N\tau_0$  under  $-\hat{\mathcal{H}}_0$ . This causes an evolution backward in time that gives the following density operator at the end of the sequence

$$\begin{aligned} \hat{\rho}_\phi(N\tau_0) \xrightarrow{(-\hat{\mathcal{H}}_0), N\tau_0} \hat{\rho}_f(2N\tau_0) &= e^{i\hat{\mathcal{H}}_0 N\tau_0} \hat{\rho}_\phi(N\tau_0) e^{-i\hat{\mathcal{H}}_0 N\tau_0} \\ &= \sum_{\Delta M} \left[ e^{i\hat{\mathcal{H}}_0 N\tau_0} \hat{\rho}_{\Delta M}(N\tau_0) e^{-i\hat{\mathcal{H}}_0 N\tau_0} \right] e^{i\Delta M \phi}. \end{aligned} \quad (13)$$

If  $\hat{I}_z$  is the NMR observable, then the signal becomes

$$\begin{aligned} \langle \hat{I}_z \rangle(\phi, 2N\tau_0) &= \text{Tr} \left\{ \hat{I}_z \hat{\rho}_f(2N\tau_0) \right\} \\ &= \text{Tr} \left\{ e^{-i\hat{\mathcal{H}}_0 N\tau_0} \hat{\rho}_0 e^{i\hat{\mathcal{H}}_0 N\tau_0} \hat{\rho}_\phi(N\tau_0) \right\} \\ &= \text{Tr} \left\{ \hat{\rho}(N\tau_0) \hat{\rho}_\phi(N\tau_0) \right\} \\ &= \sum_{\Delta M} e^{i\phi \Delta M} \text{Tr} \left\{ \hat{\rho}_{\Delta M}^2(N\tau_0) \right\} \end{aligned} \quad (14)$$

$$= \sum_{\Delta M} e^{i\phi \Delta M} A(\Delta M), \quad (15)$$

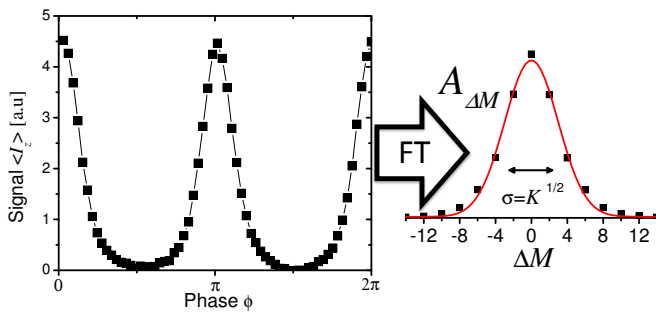


Figure 5. (Color online) Scheme for determining the MQC spectrum based on the sequence of Fig. 2. The left panel is the measured  $\langle I_z \rangle$  signal as a function of the encoding phase  $\phi$  for  $N\tau_0 = 230.4\mu\text{s}$ . After doing a Fourier transform the MQC spectrum  $A(\Delta M)$  is obtained (right panel). In the left panel, the black squares are the unperturbed signal ( $p = 0$ ), while the other colored symbols are the signal observed for a given perturbation strength  $p$ .

where  $A(\Delta M)$  are the amplitudes of the MQ spectrum shown in Fig. 3b. To extract these amplitudes from the experimental data, we measure the signal  $\langle \hat{I}_z \rangle(\phi, N\tau_0)$  as a function of  $\phi$  at a fixed time  $N\tau_0$  and then perform a Fourier transform with respect to  $\phi$  as shown schematically in Fig. 5 (Black squares). The cluster size is then determined by the half-width at  $e^{-1}$ ,  $\sigma = \sqrt{K}$ , of  $A(\Delta M)$ .

### 3. Growth of the clusters

Figure 6 shows the time evolution of the measured cluster size  $K(N\tau_0)$  as a function of the total evolution time  $N\tau_0$ . For the unperturbed Hamiltonian, the cluster size appears to grow indefinitely [35, 36]. The figure also shows two examples of the  $A(\Delta M)$  distributions at different times. We can see that for long times  $K \propto (N\tau_0)^{4.3}$ . Assuming that the cluster-size  $K$  is associated with the number of spins inside a volume, it is seen that the associated length grow faster than normal diffusion, where its growing curve would be expected to be  $\propto (N\tau_0)^{3/2}$ .

This evolution can be reversed completely by changing the Hamiltonian from  $\hat{\mathcal{H}}_0$  to  $-\hat{\mathcal{H}}_0$ . Experimentally, this is achieved by shifting the phase of all RF pulses by  $\pm\pi/2$  [61]. The signal  $\langle I_z \rangle(\phi, N\tau_0)$  at the end of the sequence of Fig. 2 is a time reversal echo for  $\phi = 0$ . This means that under ideal conditions  $\sum_M A(\Delta M, N\tau_0) = \text{const}$  and we will write  $E(N\tau_0)$  for this quantity. The indefinite growth of the cluster size, as well as the complete reversibility of the time evolution are no longer possible if the effective Hamiltonian deviates from the ideal form (7).

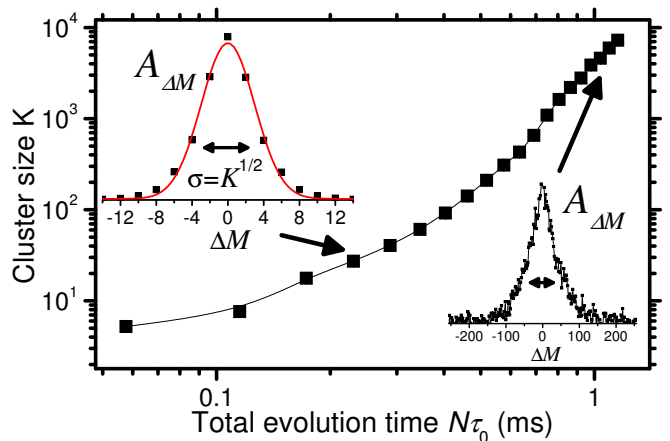


Figure 6. (Color online) Time evolution of the cluster size of correlated spins with the unperturbed Hamiltonian  $\hat{\mathcal{H}}_0$  (black squares). Distributions of the squared amplitudes  $A_{\Delta M}$  of density operator components as a function of the coherence order  $\Delta M$  are shown for two different cluster sizes.

## B. Effect of perturbations

### 1. Intrinsic perturbations

Experimentally, the Hamiltonian  $\hat{\mathcal{H}}_0$  is generated as an effective Hamiltonian by the pulse sequence of Fig. 2. Because of experimental imperfections, it always deviates from the ideal Hamiltonian (7). As a result, the actual dynamics deviates from the ideal one and, in particular, we cannot invert exactly the perturbed Hamiltonian and thus reverse the time evolution perfectly. The quantity  $\sum_{\Delta M} A(\Delta M)$  is no longer conserved, but decays with increasing evolution time.

The ideal form of the effective Hamiltonian (7) can only be created if the dipolar couplings  $d_{i,j}$  are time independent and the pulses are ideal and rotate globally all the spins. However, if these couplings are time dependent, or the pulses are not ideal, the effective Hamiltonian (averaged over the pulse cycle) contains additional terms. We have partly characterized the spectral density of local spin-spin fluctuations driven by  $\hat{\mathcal{H}}_{dd}$  in Ref. [55, 63] and its correlation time was about  $\tau_d = 110\mu\text{s}$ . Since the imperfection on  $\hat{\mathcal{H}}_0$  are correlated with the fluctuations driven by  $\hat{\mathcal{H}}_{dd}$ , we can use  $\tau_d$  to estimate the correlation time of the fluctuations of the  $\hat{\mathcal{H}}_0$  imperfections.

In Fig. 6 the cluster size grows faster for times lower than  $\tau_d$ . After  $\tau_d$  the cluster size growth reduces speed and seems to start growing exponentially [35, 36]. After 1ms, the growing law again change its behavior and the cluster size grows as a power law [35, 36]. We cannot contrast this regime with the spectral density determined in Ref. [63] because it was not determined for the corresponding range of frequency fluctuations. While all these regimes cannot be rigorously determined, there is a fact that the cluster-size keeps growing for long time

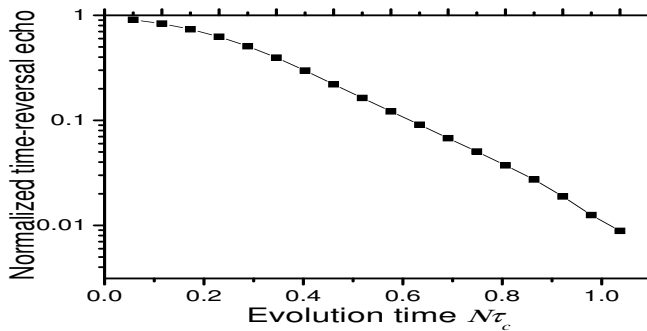


Figure 7. Time-reversal echo probability. The black squares are the unperturbed ( $p = 0$ ) echo decay  $E(N_0\tau_0)$ , measured with the sequence of Fig. 2, as a function of the evolution time  $N_0\tau_0$ . The left axis gives the time-reversal probability normalized with respect to the signal at  $N = 0$ .

and faster than normal diffusion. This ‘super-diffusion’ may be a result of the long range nature of the dipolar interaction [64, 65].

In previous works [35, 36] and in Fig. 6, we determined the cluster growth by isolating the intrinsic decay generated by an imperfect effective Hamiltonian (7). The imperfection effects are manifested in the overall decrease of the echo signal  $E(N\tau_0)$  by normalizing the MQ spectra such that the total signal  $\sum_{\Delta M} A(\Delta M)$  for  $\phi = 0$  is constant in time. Now, we measured the decay of  $E(N\tau_0) = \sum_{\Delta M} A(\Delta M, N\tau_0)$ . The results are shown in Fig. 7. If we consider the imperfections on  $\hat{H}_0$ , the effective Hamiltonian during the first part of the sequence of Fig. 2a will be  $\hat{H}_{fwd} = \hat{H}_0 + \hat{H}_e$ , and  $\hat{H}_{bwd} = -\hat{H}_0 + \hat{H}'_e$  during the time reversed part, where  $\hat{H}_e$  is an average error Hamiltonian. The echo decay is then  $E(N_0\tau_0) = \text{Tr} \{ \hat{\rho}^{\hat{H}_{fwd}}(N\tau_0) \hat{\rho}^{\hat{H}_{bwd}}(N\tau_0) \}$  and it quantifies the time reversal probability as a kind of Loschmidt echo [24, 25, 66].

The echo decay  $E(N_0\tau_0)$  shown in Fig. 7 starts as a Gaussian for times shorter than  $N_0\tau_0 \lesssim 288\mu\text{s} \approx 2.6\tau_d$ . For longer times it decays exponentially until  $\approx 920\mu\text{s}$  where a different decay law arises. These transitions between different decay laws seems to be correlated with the growing law transitions discussed in the previous paragraphs. This resembles the typical behavior of nuclear spins of a solution diffusing in a inhomogeneous magnetic field with a given standard deviation [67] or in restricted spaces in the presence of a magnetic field gradient [68]. If the spins only interact with the magnetic field, due to the diffusion process, they feel a different magnetic field at different times causing dephasing of the spin signal. The frequency fluctuations have a correlation time given by the time needed to explore the standard deviation of the changes of the magnetic field that is related with the inhomogeneity of the magnetic field or to the restriction length. By applying a spin-echo sequence -a time reversal of the spin precession by an inversion pulse that changes the sign of the magnetic field interaction- one can

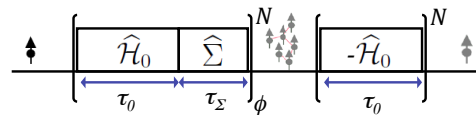


Figure 8. (Color online) Sequence for generating a perturbed evolution. It is achieved when  $\tau_\Sigma \neq 0$ , where  $\hat{\Sigma} = \hat{H}_{dd}$  is the free evolution Hamiltonian.

partly reverse the effects of the diffusion-driven dephasing [69, 70]. The echo sequence is analogous to the one of Fig. 2. If the inversion pulse inducing the time reversal is applied at times shorter than the correlation time of the frequency fluctuations of the spins, the signal decay depends of the spatial displacement of the spins and the signal decays faster as the time passes because the dephasing rate increases with the displacement length. However, for times longer than the correlation time of the frequency fluctuations the decay rate becomes independent of the displacement and becomes exponential, similar to the time reversal echo behavior shown in Fig. 7.

## 2. Controlled perturbation

The echo decay in Fig. 7 depends of perturbation  $\hat{H}_e$ . In order to study the sensitivity to the perturbation strength, we introduced a perturbation  $\hat{\Sigma}$ , whose strength we can control experimentally and study the behavior of the system as a function of the perturbation strength. We choose the raw dipole-dipole coupling for this perturbation,  $\hat{\Sigma} = \hat{H}_{dd}$ , which has long range interactions with coupling strengths decaying as  $1/r^3$ . We add this Hamiltonian to the ideal Hamiltonian  $\hat{H}_0$  by concatenating short evolution periods under  $\hat{H}_{dd}$  with evolution periods under  $\hat{H}_0$ . We label the durations of the two time periods  $\tau_\Sigma$  and  $\tau_0$ , as shown in Fig. 8. When the duration  $\tau_c = \tau_0 + \tau_\Sigma$  of each cycle is short compared to the inverse of the dipolar couplings  $d_{ij}$ , the resulting evolution can be described by the effective Hamiltonian

$$\hat{H}_{\text{eff}} = (1 - p)\hat{H}_0 + p\hat{\Sigma}, \quad (16)$$

where the relative strength  $p = \tau_\Sigma/\tau_c$  of the perturbation  $\hat{\Sigma} = \hat{H}_{dd}$  can be controlled by adjusting the duration  $\tau_\Sigma$ . For the quantum simulations, we compared the artificially perturbed evolution of  $\hat{H}_{\text{eff}}$  with the  $\hat{H}_0$  evolution with its intrinsic errors. While the intrinsic errors reduce the signal or the overall fidelity, they do not cause localization on the time scale of our experiments (see Fig. 6).

Starting from thermal equilibrium, now the state of the system at the end of  $N$  cycles is  $\hat{\rho}^{\hat{H}_{\text{eff}}}(N\tau_c) = e^{-i\hat{H}_{\text{eff}}N\tau_c} \hat{\rho}_0 e^{i\hat{H}_{\text{eff}}N\tau_c}$ . Taking into account now the complete sequence of evolutions given by Fig. 2b, the experiment is thus a perturbed forward evolu-

tion and an unperturbed backward evolution. The density matrix at the end of the sequence is then  $\sum_M \left[ e^{i\hat{\mathcal{H}}_0 N\tau_0} \hat{\rho}_M^{\mathcal{H}_{\text{eff}}} (N\tau_c) e^{-i\hat{\mathcal{H}}_0 N\tau_0} \right] e^{iM\phi}$  as derived in [35, 36]. Thus the NMR echo signal, which is measured after the last backward evolution  $\exp \left\{ i\hat{\mathcal{H}}_0 N\tau_0 \right\}$ , can be written as

$$\begin{aligned} \langle I_z \rangle (\phi, N\tau_c) &= \text{Tr} \left\{ \hat{I}_z \hat{\rho}_f (N\tau_c + N\tau_0) \right\} \\ &= \text{Tr} \left\{ \hat{\rho}^{\mathcal{H}_0} (N\tau_0) \hat{\rho}_\phi^{\mathcal{H}_{\text{eff}}} (N\tau_c) \right\}. \end{aligned} \quad (17)$$

In terms of the individual MQ coherences, this may be written as

$$\langle I_z \rangle (\phi, N\tau_c) = \sum_{\Delta M} e^{i\phi\Delta M} \text{Tr} \left\{ \hat{\rho}_{\Delta M}^{\mathcal{H}_0} (N\tau_0) \hat{\rho}_{\Delta M}^{\mathcal{H}_{\text{eff}}} (N\tau_c) \right\} \quad (18)$$

with the MQ coherence amplitudes  $A(\Delta M) = \text{Tr} \left\{ \hat{\rho}_{\Delta M}^{\mathcal{H}_0} (N\tau_0) \hat{\rho}_{\Delta M}^{\mathcal{H}_{\text{eff}}} (N\tau_c) \right\}$ . For the ideal evolution ( $p = 0$ ), Eq. (14) is recovered, where  $A(\Delta M)$  correspond to the squared amplitudes of the density operator elements  $\hat{\rho}_{\Delta M}^{\mathcal{H}_0} (N\tau_0)$  with coherence order  $\Delta M$ . For the perturbed evolution, ( $p \neq 0$ ), they are reduced by the overlap of the actual density operator elements  $\hat{\rho}_{\Delta M}^{\mathcal{H}_{\text{eff}}} (N\tau_c)$  with the ideal ones. We extract these amplitudes by performing a Fourier transformation with respect to  $\phi$ . Figure 9 shows a comparison between the distributions  $A(\Delta M)$  for different evolution times for an unperturbed evolution (panel a) and a perturbed evolution with  $p = 0.108$  (panel b). The main difference is that the MQC spectrum of the perturbed evolution does not spread indefinitely but its width reaches a limiting value [35, 36].

As discussed in section III A 2, we determine the cluster size for different evolution times and perturbation strengths from the width of the measured MQC distributions. Figure 10 shows the cluster size (the number of correlated spins) as a function of the evolution time  $N\tau_c$ . The main difference of the perturbed time evolutions (colored symbols in Fig. 10) compared to the unperturbed evolution (black squares) is that the cluster size does not grow indefinitely [35, 36], but saturates. It remains unclear if the cluster growth for the weakest perturbation  $p = 0.009$  also saturates. We consider this saturation as evidence of localization due to the perturbation and the localization size decreases with increasing the perturbation strength  $p$ .

### C. Quantum dynamics from different initial cluster sizes

We have shown that time evolution of the cluster size under perturbations reaches a dynamical equilibrium state [35, 36], i.e. for a given perturbation strength, the size of the spin clusters tends toward the same limiting value, independent of the initial condition. In order to

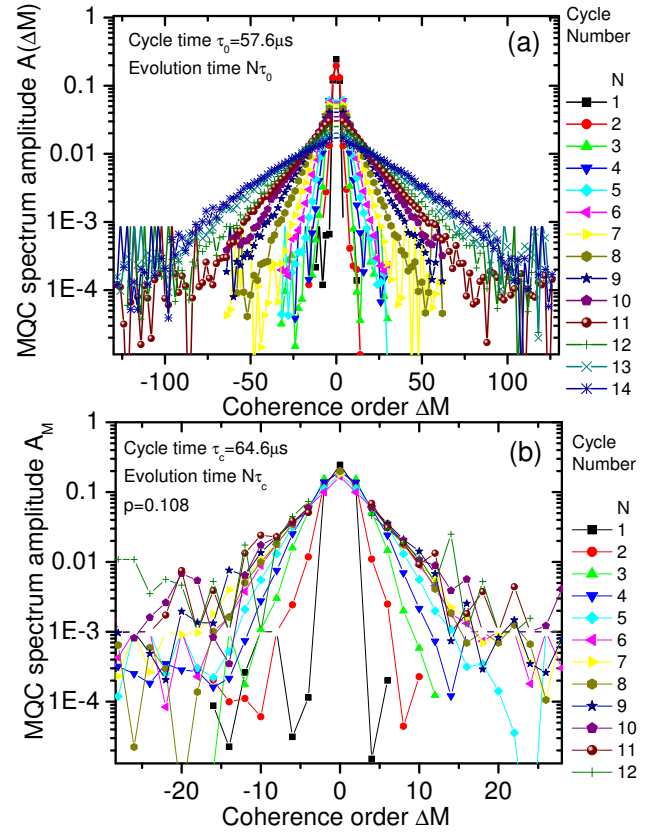


Figure 9. (Color online) MQC spectra for different evolution times and perturbation strengths. Panel (a) shows the  $A(\Delta M)$  spectrum for the unperturbed evolution ( $p = 0$ ) for different times. Panel (b) shows its analogous but for  $p = 0.108$ . Panel (b) shows manifestation of the localization effects evidenced on the saturation of the spreading of the MQC spectrum.

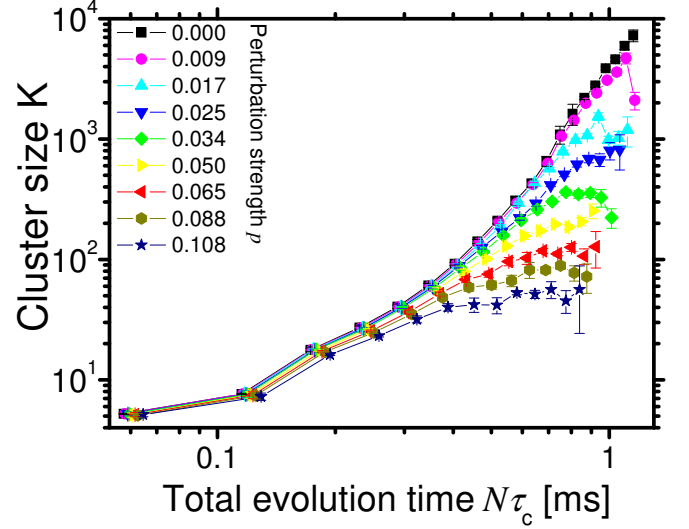


Figure 10. (Color online) Time evolution of the cluster size  $K$  for different perturbation strengths. The cluster size is related to the volume occupied by the  $K$  spins. By increasing the perturbation, the localization-size is reduced.

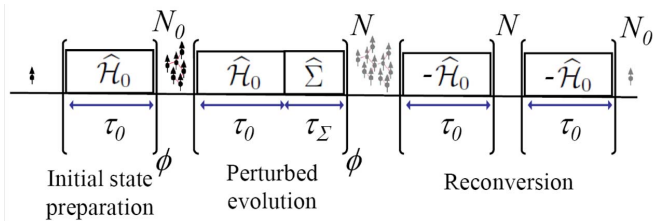


Figure 11. (Color online) Sequence for preparing different initial cluster sizes by controlling  $N_0$  and subsequently evolving them in the presence of a perturbation.

show this, we prepared a series of initial conditions corresponding to different cluster sizes. Figure 11 shows the corresponding pulse sequence: The initial state preparation, consisting of an evolution of duration  $N_0\tau_0$  under the unperturbed Hamiltonian  $\hat{H}_0$ , generates clusters of size  $K_0$ .

During the subsequent perturbed evolution of duration  $N\tau_c$ , these initial clusters evolve and Eq. (17) becomes

$$\langle I_z \rangle (\phi, N_0\tau_0 + N\tau_c) = \text{Tr} \left\{ \hat{\rho}^{\mathcal{H}_0} (N\tau_0, N_0\tau_0) \hat{\rho}_\phi^{\mathcal{H}_{\text{eff}}} (N\tau_c, N_0\tau_0) \right\}. \quad (19)$$

This method allows us to study the growth of the clusters by starting from different sizes  $K_0 = K(N_0\tau_0)$  and following the evolution as a function of time and perturbation strength. Based on Eq. (19), we determined the MQC spectra  $A(\Delta M)$  for different evolution times. The insets of Fig. 12, shows two examples of them. From such curves, we determined the evolution of the cluster size shown in Fig. 12. The figure shows evolution of the cluster size for two perturbation strengths, starting from different initial sizes. The dynamical equilibrium is clearly manifested in the figure. The two insets show the  $A(\Delta M)$  spectrums starting from  $K_0 = 141$ , for different evolution times. We can see that if  $K_0$  is lower than the localization size, the MQC spectrum spreads until it localizes (manifested by the parallel slopes), however if  $K_0$  is larger than the localization size, it shrink until saturation. We found that the localization size vs. the perturbation strength is roughly proportional to  $1/p^2$  [35, 36]. During our experiment, the magnetization is uniform throughout the sample, so the process does not lead to a spatial redistribution of magnetization. Note however that here we measure the cluster size of correlated spins that is associated with a coherent length. Therefore, this technique allows to investigate the localization size, even when the density profile of the excited cluster size would exceed the localization length.

#### IV. CONCLUSIONS

As a step toward the understanding of the quantum evolution of large quantum systems, we have studied the

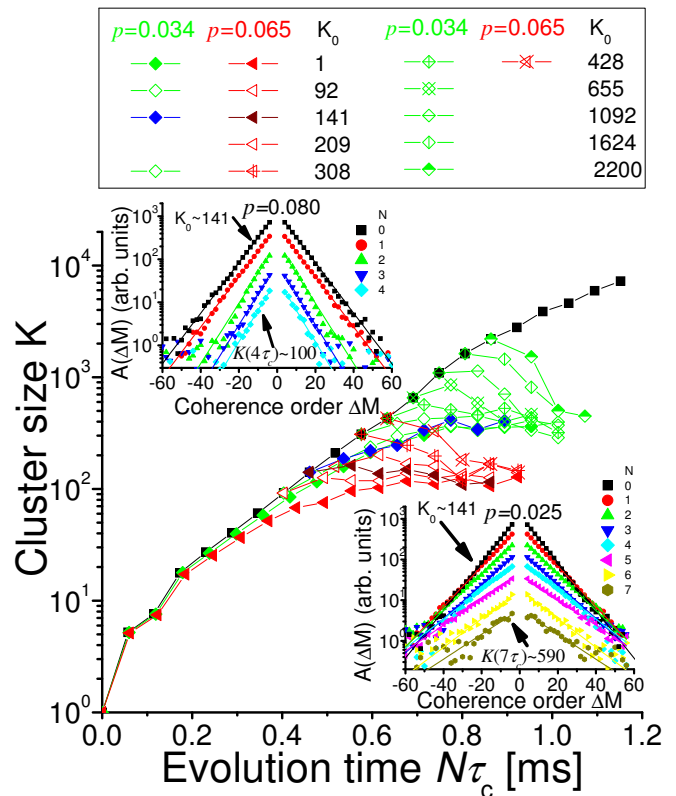


Figure 12. (Color online) Time evolution of the cluster-size of correlated spins starting from different initial states. The experimental data is shown for two different perturbation strengths given in the legend. The solid black squares, red triangles and green rhombuses are evolutions from an uncorrelated initial state. Empty symbols start from an initial state with  $K_0$  correlated spins (see legend). The solid blue rhombuses and brown triangles starts from an initial  $K_0 = 141$ . The insets show the MQC spectrum starting from  $K_0 = 141$  as a functions of time for the two perturbation strengths.

spreading of information in a system of nuclear spins. Decoherence has long been recognized to limit the time for which quantum information can be used. Spatial disorder also limits the distance over which quantum information can be transferred. We have studied the role of a disordered dipolar interaction Hamiltonian and shown that for larger values of the perturbation, the coherence length of the cluster size reaches a limit value. Even though we do not measure directly the spatial extent of the cluster size, one might speculate that the spatial extent and the number of correlated spins are related with  $\text{Volume} \sim K$ . A connection to Anderson localization of spins with dipolar  $1/r^3$  interactions could thus be explored [29, 31, 32, 34, 39, 40]. We also note that for lower values of the perturbation, the size of the cluster grows faster than expected for a diffusive model. We will investigate possible connections to Levy flights and Levy walks induced by the long range dipole-dipole couplings of our Hamiltonians. We developed a method that allows one to quantify the time evolution of the cluster size of

correlated spins starting with single qubits. As we have shown, the information can spread to clusters of several thousand qubits. We have observed that the combination of an information spreading Hamiltonian and a perturbation to it results in a quantum state that becomes localized. The localization size decreases with increasing strength of the perturbation and the resulting size appears to be determined by a dynamic equilibrium [35, 36], a feature which might be adapted to other communities studying Anderson localization.

The results presented here provide information about the spatial bounds for transferring quantum information in large spin networks and indicate how precise manipu-

lations of large quantum systems have to be. The sample used in this study is also an interesting system for studying fundamental aspects of Anderson localization in the presence of long range interactions.

## ACKNOWLEDGMENTS

This work was supported by the DFG through Su 192/24-1. G.A.A. acknowledges financial support from the Alexander von Humboldt Foundation and from the European Commission under the Marie Curie Intra-European Fellowship.

- 
- [1] T. D. Ladd, F. Jelezko, R. Laflamme, Y. Nakamura, C. Monroe, and J. L. O'Brien, *Nature* **464**, 45 (2010).
- [2] D. P. DiVincenzo, *Science* **334**, 50 (2011).
- [3] J. Simon, W. S. Bakr, R. Ma, M. E. Tai, P. M. Preiss, and M. Greiner, *Nature* **472**, 307 (2011).
- [4] A. Aspuru-Guzik and P. Walther, *Nat. Phys.* **8**, 285 (2012).
- [5] R. Blatt and C. F. Roos, *Nat. Phys.* **8**, 277 (2012).
- [6] I. Bloch, J. Dalibard, and S. Nascimbene, *Nat. Phys.* **8**, 267 (2012).
- [7] A. A. Houck, H. E. Türeci, and J. Koch, *Nat. Phys.* **8**, 292 (2012).
- [8] T. Schulz, R. Ritz, A. Bauer, M. Halder, M. Wagner, C. Franz, C. Pfleiderer, K. Everschor, M. Garst, and A. Rosch, *Nat. Phys.* **8**, 301 (2012).
- [9] P. W. Shor, in *Proceedings of the 35th Annual Symposium on the Foundations of Computer Science*, edited by S. Goldwasser (IEEE Computer Society Press, Los Alamitos, CA, 1994) p. 124.
- [10] D. P. DiVincenzo, *Science* **270**, 255 (1995).
- [11] M. A. Nielsen and I. L. Chuang, *Quantum Computation and Quantum Information* (Cambridge University Press, Cambridge, 2000).
- [12] P. Hauke, F. M. Cucchietti, L. Tagliacozzo, I. Deutsch, and M. Lewenstein, *Rep. Prog. Phys.* **75**, 082401 (2012).
- [13] T. Monz, P. Schindler, J. T. Barreiro, M. Chwalla, D. Nigg, W. A. Coish, M. Harlander, W. Hensel, M. Hennrich, and R. Blatt, *Phys. Rev. Lett.* **106**, 130506 (2011).
- [14] H. D. Raedt and K. Michielsen, quant-ph/0406210. Handbook of Theoretical and Computational Nanotechnology. Quantum and Molecular Computing, Quantum Simulations (American Scientific Publishers, 2006). (2004).
- [15] W. Zhang, N. Konstantinidis, K. A. Al-Hassanieh, and V. V. Dobrovitski, *J. Phys.: Condens. Matter* **19**, 083202 (2007).
- [16] S. Popescu, A. J. Short, and A. Winter, *Nat Phys* **2**, 754 (2006).
- [17] G. A. Álvarez, E. P. Danieli, P. R. Levstein, and H. M. Pastawski, *Phys. Rev. Lett.* **101**, 120503 (2008).
- [18] H. G. Krojanski and D. Suter, *Phys. Rev. Lett.* **93**, 090501 (2004).
- [19] H. G. Krojanski and D. Suter, *Phys. Rev. Lett.* **97**, 150503 (2006).
- [20] M. Lovric, H. Krojanski, and D. Suter, *Phys. Rev. A* **75**, 042305 (2007).
- [21] W. S. Bakr, J. I. Gillen, A. Peng, S. Fölling, and M. Greiner, *Nature* **462**, 74 (2009).
- [22] M. Endres, M. Cheneau, T. Fukuhara, C. Weitenberg, P. Schauß, C. Gross, L. Mazza, M. C. Bañuls, L. Pollet, I. Bloch, and S. Kuhr, *Science* **334**, 200 (2011).
- [23] W. H. Zurek, *Rev. Mod. Phys.* **75**, 715 (2003).
- [24] H. M. Pastawski, P. R. Levstein, G. Usaj, J. Raya, and J. A. Hirschinger, *Physica A* **283**, 166 (2000).
- [25] R. A. Jalabert and H. M. Pastawski, *Phys. Rev. Lett.* **86**, 2490 (2001).
- [26] H. Cho, P. Cappellaro, D. G. Cory, and C. Ramanathan, *Phys. Rev. B* **74**, 224434 (2006).
- [27] C. M. Sánchez, H. M. Pastawski, and P. R. Levstein, *Physica B* **398**, 472 (2007).
- [28] A. Zwick, G. A. Álvarez, J. Stolze, and O. Osenda, *Phys. Rev. A* **85**, 012318 (2012).
- [29] A. Pomeransky and D. Shepelyansky, *Phys. Rev. A* **69**, 014302 (2004).
- [30] G. D. Chiara, D. Rossini, S. Montangero, and R. Fazio, *Phys. Rev. A* **72**, 012323 (2005).
- [31] J. Keating, N. Linden, J. Matthews, and A. Winter, *Phys. Rev. A* **76**, 012315 (2007).
- [32] C. K. Burrell and T. J. Osborne, *Phys. Rev. Lett.* **99**, 167201 (2007).
- [33] T. Apollaro and F. Plastina, *Open Systems & Information Dynamics* **14**, 41 (2007).
- [34] J. Allcock and N. Linden, *Phys. Rev. Lett.* **102**, 110501 (2009).
- [35] G. A. Álvarez and D. Suter, *Phys. Rev. Lett.* **104**, 230403 (2010).
- [36] G. A. Álvarez and D. Suter, *Phys. Rev. A* **84**, 012320 (2011).
- [37] G. A. Álvarez, E. P. Danieli, P. R. Levstein, and H. M. Pastawski, *Phys. Rev. A* **82**, 012310 (2010).
- [38] A. Zwick, G. A. Álvarez, J. Stolze, and O. Osenda, *Phys. Rev. A* **84**, 022311 (2011).
- [39] P. W. Anderson, *Phys. Rev.* **109**, 1492 (1958).
- [40] P. W. Anderson, *Rev. Mod. Phys.* **50**, 191 (1978).
- [41] H. Hu, A. Strybulevych, J. H. Page, S. E. Skipetrov, and B. A. van Tiggelen, *Nat. Phys.* **4**, 945 (2008).
- [42] J. Chabe, G. Lemarié, B. Grémaud, D. Delande, P. Szriftgiser, and J. C. Garreau, *Phys. Rev. Lett.* **101**, 255702 (2008).

- [43] S. S. Kondov, W. R. McGehee, J. J. Zirbel, and B. De-Marco, *Science* **334**, 66 (2011).
- [44] F. Jendrzejewski, A. Bernard, K. Müller, P. Cheinet, V. Josse, M. Piraud, L. Pezzetti, L. Sanchez-Palencia, A. Aspect, and P. Bouyer, *Nat. Phys.* **8**, 398 (2012).
- [45] T. Sperling, W. Buhrer, C. M. Aegerter, and G. Maret, *Nature Photonics* **7**, 48 (2013).
- [46] I. L. Aleiner, B. L. Altshuler, and K. B. Efetov, *Phys. Rev. Lett.* **107**, 076401 (2011).
- [47] L. Viola, E. Knill, and S. Lloyd, *Phys. Rev. Lett.* **82**, 2417 (1999).
- [48] D. A. Lidar, I. L. Chuang, and K. B. Whaley, *Phys. Rev. Lett.* **81**, 2594 (1998).
- [49] J. Preskill, *Proc. R. Soc. Lond. A* **454**, 385 (1998).
- [50] E. Knill, *Nature* **434**, 39 (2005).
- [51] E. M. Fortunato, L. Viola, M. A. Pravia, E. Knill, R. Laflamme, T. F. Havel, and D. G. Cory, *Phys. Rev. A* **67**, 062303 (2003).
- [52] T. Monz, K. Kim, A. S. Villar, P. Schindler, M. Chwalla, M. Riebe, C. F. Roos, H. Häffner, W. Hansel, M. Hennrich, and R. Blatt, *Phys. Rev. Lett.* **103**, 200503 (2009).
- [53] M. J. Biercuk, H. Uys, A. P. VanDevender, N. Shiga, W. M. Itano, and J. J. Bollinger, *Nature* **458**, 996 (2009).
- [54] J. Du, X. Rong, N. Zhao, Y. Wang, J. Yang, and R. B. Liu, *Nature* **461**, 1265 (2009).
- [55] G. A. Álvarez, A. Ajoy, X. Peng, and D. Suter, *Phys. Rev. A* **82**, 042306 (2010).
- [56] A. M. Souza, G. A. Alvarez, and D. Suter, *Phys. Rev. Lett.* **106**, 240501 (2011).
- [57] A. M. Souza, J. Zhang, C. A. Ryan, and R. Laflamme, *Nat. Commun.* **2**, 169 (2011).
- [58] C. P. Slichter, *Principles of Magnetic Resonance*, 2nd ed. (Springer-Verlag, 1992).
- [59] T. Lahaye, C. Menotti, L. Santos, M. Lewenstein, and T. Pfau, *Rep. Prog. Phys.* **72**, 126401 (2009).
- [60] M. Saffman, T. G. Walker, and K. Molmer, *Rev. Mod. Phys.* **82**, 2313-2363 (2010).
- [61] W. Warren, S. Sinton, D. Weitekamp, and A. Pines, *Phys. Rev. Lett.* **43**, 1791 (1979).
- [62] J. Baum, M. Munowitz, A. N. Garroway, and A. Pines, *J. Chem. Phys.* **83**, 2015 (1985).
- [63] G. A. Álvarez and D. Suter, *Phys. Rev. Lett.* **107**, 230501 (2011).
- [64] R. Metzler and J. Klafter, *Physics Reports* **339**, 1 (2000).
- [65] N. Mercadier, W. Guerin, M. Chevrollier, and R. Kaiser, *Nat. Phys.* **5**, 602 (2009).
- [66] W. K. Rhim, A. Pines, and J. S. Waugh, *Phys. Rev. Lett.* **25**, 218 (1970).
- [67] J. R. Klauder and P. W. Anderson, *Phys. Rev.* **125**, 912 (1962).
- [68] R. P. Kennan, J. Zhong, and J. C. Gore, *Magn. Reson. Med.* **31**, 9 (1994).
- [69] E. Hahn, *Phys. Rev.* **80**, 580 (1950).
- [70] H. Carr and E. Purcell, *Phys. Rev.* **94**, 630 (1954).